Rubidium Fluoride Absorber Treatment for Wide-Gap (Ag,Cu)(In,Ga)Se<inf>2</inf> Solar Cells

Citation for the original published paper (version of record):
Keller, J., Aboulfadl, H., Stolt, L. et al (2022). Rubidium Fluoride Absorber Treatment for Wide-Gap (Ag,Cu)(In,Ga)Se<inf>2</inf> Solar Cells. Solar RRL, 6(6).
http://dx.doi.org/10.1002/solr.202200044

Rubidium Fluoride Absorber Treatment for Wide-Gap (Ag,Cu)(In,Ga)Se_2 Solar Cells

Jan Keller, Hisham Aboulfadl, Lars Stolt, Olivier Donzel-Gargand, and Marika Edoff*

This contribution studies the potential of an RbF postdeposition treatment (RbF-PDT) of wide-gap (Ag,Cu)(In,Ga)Se_2 (ACIGS) absorbers to improve the corresponding solar cell performance. While a higher open-circuit voltage (V_{OC}) and short-circuit current density are achieved, a lower fill factor (FF) is observed for most of the devices subjected to an RbF-PDT. However, the drop in FF can be avoided for some close-stoichiometric samples, leading to maximum efficiencies beyond 16% (without antireflection coating) at a bandgap energy (E_g) of 1.43 eV. For off-stoichiometric ACIGS, a record V_{OC} value of 926 mV at $E_g = 1.44$ eV is reached. Lower V_{OC} deficits likely require enhanced bulk quality of wide-gap chalcopyrite absorbers. Extensive material analysis shows that the heavy alkali PDT of ACIGS with high Ag and Ga contents leads to similar absorber modifications as commonly observed for low-gap Cu(In,Ga)Se_2 (CIGS). Rubidium is continuously distributed at "internal" (grain boundaries) and "external" (buffer and back contact) absorber interfaces. The results indicate that Rb diffusion into the absorber bulk (including 1:1:2 and 1:3:5 compounds) is restricted. Furthermore, the formation of a very thin $RbInSe_2$ surface layer is suggested. It remains open, which effects alter the device characteristics after RbF-PDT.

1. Introduction

To fully exploit the potential of a 2-junction photovoltaic (PV) tandem device, the top cell should exhibit an absorber bandgap energy (E_g) above 1.4 eV in a 4-terminal and $E_g \approx 1.6$ eV in a 2-terminal configuration.[1,2] Such high bandgaps can be reached for Cu(In,Ga)Se_2 (CIGS) films with [Ga]/([Ga]+[In]) (GGI) values > 0.6. However, while efficiencies (η) of CIGS-based solar cells exceed 22% for GGI values ≤ 0.3,[3,4] a distinctly inferior performance is observed for wide-gap chalcopyrite solar cells with higher Ga contents (i.e., $E_g > 1.2$ eV).[5] The most prominent bottleneck is the increasing open-circuit voltage (V_{OC}) deficit with respect to the bandgap energy. While some of the large V_{OC} loss of wide-gap chalcopyrite solar cells can be mitigated by using alternative (i.e., not CdS) buffer layers with tunable electron affinity (χ),[6–10] a major part of the deficit seems to arise from a poorer bulk quality.[11,12] The lifetime deterioration with increasing GGI was suggested to originate from higher Shockley–Read–Hall (SRH) recombination via 1) energetically deeper Ga_{Cu} antisite donor defects[13–16] or (V_{Se}–V_{Cu}) complexes in acceptor state[17]; 2) an increasing density of deep acceptors[18,19]; 3) an increasing tetragonal lattice distortion[20]; and/or 4) an increased fraction of Cu-enriched (supposedly detrimental[21]) grain boundaries (GBs).[22]

Instead of utilizing low-χ alternative buffers, interface recombination can also be reduced (or canceled out) for CdS-buffered wide-gap CIGS solar cells when the absorber is alloyed with silver, i.e., forming (Ag,Cu)(In,Ga)Se_2 (ACIGS). While a detrimental negative conduction band offset (CBO) at the CdS/CIGS interface is predicted for GGI > 0.5,[23–25] sufficient Ag-alloying allows to avoid a negative CBO in the entire compositional range of ACIGS (i.e., even for GGI $= 1$).[7,26,27] Consequently, high V_{OC} values close to 900 mV and beyond were achieved for wide-gap ACIGS solar cells with CdS buffer layers by several groups.[7,11,28–32] However, it was reported that the chalcopyrite single-phase region of the ACIGS system is narrowing toward GGI and AAC $= 1$ (i.e., $AgGaSe_2$).[33] As a result, a high volume share of ordered vacancy compound (OVC) patches is observed, which significantly increases for AAC and GGI > 0.5.[7,31,34,35] While OVCs at the back contact very likely cause a kink in current–voltage (I–V) characteristics and thus a low fill factor (FF), it is currently not clear whether their occurrence at the heterojunction is beneficial, detrimental, or benign.[11,31] Further studies are ongoing to investigate the effect of the OVC patches on the electrical and optical properties of the ACIGS devices.

Recently, we revealed a clear anticorrelation between V_{OC} and the short-circuit current density (J_{SC}) with varying group-I stoichiometry for wide-gap ACIGS solar cells.[11] Perfect carrier collection (high J_{SC}) is only achieved for very close-stoichiometric compositions, due to a complete depletion of the absorber

---

J. Keller, L. Stolt, O. Donzel-Gargand, M. Edoff
Ångström Solar Center
Division of Solar Cell Technology
Uppsala University
75121 Uppsala, Sweden
E-mail: jan.keller@angstrom.uu.se

H. Aboulfadl
Division of Microstructure Physics
Department of Physics
Chalmers University of Technology
41296 Göteborg, Sweden

The ORCID identification number(s) for the author(s) of this article can be found under https://doi.org/10.1002/solr.202200044.

DOI: 10.1002/solr.202200044

(i.e., low doping). By contrast, absorbers with [I]/[III] < 0.9 show "common" doping densities and space charge region widths ($<$550 nm), resulting in higher V_{OC} and significantly lower J_{SC} values. The strong reduction in carrier collection for not fully depleted absorbers highlights the very low diffusion length and high bulk recombination, which may ultimately limit the V_{OC} of wide-gap ACIGS solar cells.

In an attempt to enhance the electron lifetime in the wide-gap ACIGS absorber, and thereby increase J_{SC} and V_{OC} of corresponding solar cells, this study investigates the potential of an RbF post-deposition treatment (RbF-PDT). The potentially beneficial effect of a heavy alkali (K, Rb, or Cs) PDT of low-gap CIGS solar cells was first reported in 2013.[36] One advantage is that it allows growing substantially thinner CdS layers, resulting in higher J_{SC} values without experiencing a loss in V_{OC} and FF. Suggested explanations are a facilitated Cd in-diffusion (creating type inversion)[36,37] or an earlier formation of a fully covering CdS layer during chemical bath deposition (CBD).[38,39] Besides the higher J_{SC}, also higher V_{OC} values are frequently observed.[3,40–43] The reason for the gain in V_{OC} is, however, still under debate. Proposed explanations are 1) surface passivation by the formation of an alkali-containing wide-gap (Alkali,Cu)–(In,Ga)–Se surface layer (presumably with openings)[44–49]; 2) mitigation/suppression of GB recombination via reduction or passivation of charged defects in GBs[50–52]; 3) increased absorber doping[53–55] (lower doping was observed as well[56]); 4) reduced concentration of deep defects[57,58] (deemed unlikely by others[50]); and 5) lower potential fluctuations.[59] Obviously, the situation remains complex and a comprehensive understanding is still lacking.

Most heavy alkali PDT experiments were conducted on low-gap, high-efficiency devices. Only very few attempts were made on wide-gap (A)CIGS solar cells. Zahedi-Azad et al. showed that KF-, RbF-, and CsF-PDTs can lead to an improved V_{OC} and efficiency for CIGS solar cells with a GGI up to about 0.8,[60] but claimed that interface recombination is still limiting. On the other hand, an RbF-PDT did not show a clear improvement in device performance for pure $CuGaSe_2$ in an another study.[61]

This contribution investigates the effect of an RbF-PDT of ACIGS absorbers in the compositional range of GGI = 0.69–0.74, [Ag]/([Ag]+[Cu]) (AAC) = 0.46–0.71, and [I]/[III] = 0.77–0.98. This composition is chosen because a positive CBO at the ACIGS/CdS interface is expected and the substantial formation of OVCs can be curbed.[7,11,31] The *I–V* parameters of corresponding solar cells (all using CdS as a buffer) will be compared with those from a large number of devices with very similar composition but without PDT, which were already presented in an earlier publication.[11] In the second part, the chemical and morphological absorber modifications introduced by the RbF-PDT are illustrated and possible impacts on device characteristics discussed.

2. Results and discussion

2.1. Impact of the RbF-PDT on Solar Cell Performance

In total, 13 absorber deposition runs (each with four samples of varying composition) with subsequent RbF-PDTs (in Se atmosphere, no prior air exposure) were conducted. After removing all group-I rich samples, 44 samples (with different GGI, AAC, and [I]/[III] values) could be extracted and analyzed from these 13 runs. For more information about the lateral spread in composition within each ACIGS deposition, we refer to.[11]

Figure 1 compares the *I–V* parameters of the best solar cells of each sample with and without PDT as a function of E_g. The respective bandgap energy depends on the exact composition[62] and was calculated using a formula presented in the study by Keller et al.[7] Resulting E_g values are very close to the ones extracted experimentally from external quantum efficiency (EQE) measurements. The color code illustrates the corresponding [I]/[III] value for each sample and the dashed gray lines represent E_g values with constant percentage of the theoretical Shockley–Queisser (SQ) maximum for J_{SC} and V_{OC},[63] respectively. It is evident that the RbF-PDT leads to (on average) higher V_{OC} values, with $\Delta V_{OC} \approx +25$ mV for the best samples at $E_g = 1.42$–1.45 eV. As was found for cells without PDT, V_{OC} also increases with decreasing [I]/[III] value when an RbF-PDT is applied. This behavior was ascribed to an increasing doping density with increasing group-I off-stoichiometry, which saturates for [I]/[III] < 0.90.[11] The results indicate that the doping versus stoichiometry relationship is not significantly altered by the PDT. A comparison of corresponding trends in space charge region width, as deduced by capacitance–voltage (*C–V*) profiling, confirms this (see Figure S1 in the Supporting Information).

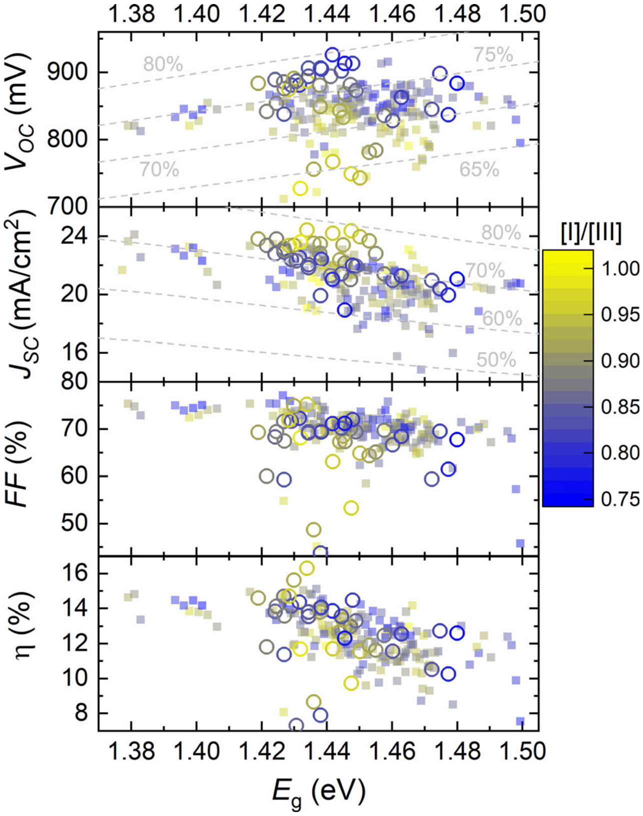

Figure 1. Solar cell parameters (best cells) as a function of bandgap energy, extracted from *I–V* analysis. Squares represent samples without, circles samples with RbF-PDT, and the color code shows the corresponding cation ratio. The dashed gray lines illustrate E_g values with constant percentage of the theoretical maximum in J_{SC} and V_{OC}, respectively.

Furthermore, the beneficial effect of the RbF-PDT seems to be independent of the [I]/[III] value.

The RbF-PDT allowed to use thinner CdS layers (44 nm), as compared to samples without PDT (57 nm), without experiencing V_{OC} losses. The corresponding reduction in parasitic absorption leads to a gain in J_{SC} of about 0.7 mA cm^{-2}. This explains a part of the higher J_{SC} values (all deduced from EQE measurements) for samples subjected to an RbF-PDT. However, the average J_{SC} gain is slightly larger (see Figure 1), which may be the result of an improved carrier lifetime after the PDT. Again, as was previously observed for samples without PDT,[11] the carrier collection is increasing toward stoichiometric absorber composition ([I]/[III] $\approx$ 0.97). A full depletion is still required to avoid collection losses, which implies that the bulk properties are not sufficiently improved by the RbF treatment.

While V_{OC} and J_{SC} can be increased, the FF is slightly reduced for most of the samples when an RbF-PDT is applied. Possible reasons will be discussed in the next paragraph. The lower FF compensates the gain in V_{OC} and J_{SC} in the majority of cases, resulting in no clear overall efficiency improvement by the PDT. However, for two close-stoichiometric samples ([I]/[III] = 0.93 and 0.96) a high FF could be maintained. The corresponding best solar cells show efficiencies of 15.6% and 16.3% at $E_g = 1.43$ eV, without antireflection coating (ARC). The *I–V* characteristic and EQE spectrum of the best solar cell (GGI = 0.70, AAC = 0.61, and [I]/[III] = 0.96) are presented in **Figure 2**.

For comparison, the data of a solar cell with similar composition (GGI = 0.68, AAC = 0.66, and [I]/[III] = 0.97), but without a PDT, are added as well. For these particular samples, the difference in V_{OC} is 58 mV. Both samples show very high and squared EQE curves, indicating negligible collection losses as a result of the very wide space charge region that establishes for close-stoichiometric absorber compositions.[11] The decreasing EQE values toward short wavelengths for the sample with PDT are caused by reflection losses. This is evident when considering the shape of the EQE curve after applying an MgF_2 ARC (also added in Figure 2b)). Unfortunately, the V_{OC} and FF degraded between the initial cell characterization and the time when the MgF_2 was deposited (3 months in N_2 cabinet). Without this degradation, the increased J_{SC} would have resulted in an efficiency of at least 17.2% with ARC. The nature of the degradation is currently under investigation, but seems to be independent of the RbF-PDT step. Possible origins may be the redistribution/migration of mobile ions (most likely Na), change in electronic defect density/energy/configuration, or even (but less likely) phase decomposition during long-term storage. In addition, an effect of a potential ingress of atmospheric species/moisture (which would be suppressed by an encapsulation in a final module) cannot be excluded. A separate publication is planned for the near future.

Figure 3 shows the V_{OC} and FF trends as a function of the GGI value. In the upper row, the color code represents the AAC and in the lower row the [I]/[III] value. Summarizing all samples, it may be concluded that (apart from a few outliers) the best V_{OC} values start to saturate at about 900 mV for GGI > 0.70. However, more data points with GGI > 0.75 are needed for the RbF-PDT samples to confirm this statement. Variations in Ag content in the investigated range do not have a significant impact on the achievable V_{OC} (see differences in [I]/[III]). At the same GGI of about 0.70, the FF values tend to decrease, making it challenging to reach high efficiencies for higher E_g. It is suggested that the electron lifetime is considerably decreasing for GGI > 0.7, presumably by a shifting energy of the Ga_I defect further away from the conduction band minimum.[13–16] As a result, bulk recombination ultimately limits V_{OC} and voltage-dependent current collection reduces FF for GGI > 0.7. However, an additional (but presumably small) contribution by an increasing interface recombination with increasing GGI (i.e., decreasing CBO) cannot be excluded. If this hypothesis is true, Ag-alloying indeed reduces interface recombination for wide-gap chalcopyrite solar cells when a CdS buffer layer is used (positive CBO), but it does not improve the bulk properties, which sets an upper limit to the V_{OC} and FF values.

The highest V_{OC} of 926 mV was reached when applying an RbF-PDT to an absorber with a composition of GGI = 0.74, AAC = 0.45, and [I]/[III] = 0.80 and $E_g = 1.44$ eV. For close-stoichiometric compositions [I]/[III] > 0.90, a V_{OC} greater than 891 mV could not be reached. **Figure 4** sets this V_{OC} number (labeled "RbF") into perspective with the highest reported values for solar cells with different chalcopyrite compositions (including sulfur), with resulting bandgaps varying from 1.0 to 1.7 eV (dots and stars). For comparison, also the best V_{OC}–E_g pairs of other technologies are added. The data were extracted from previous studies[4–9,28,29,31,60,64–77] (not claiming completeness). Alternative, low-χ buffers only lead to a significant V_{OC} gain over

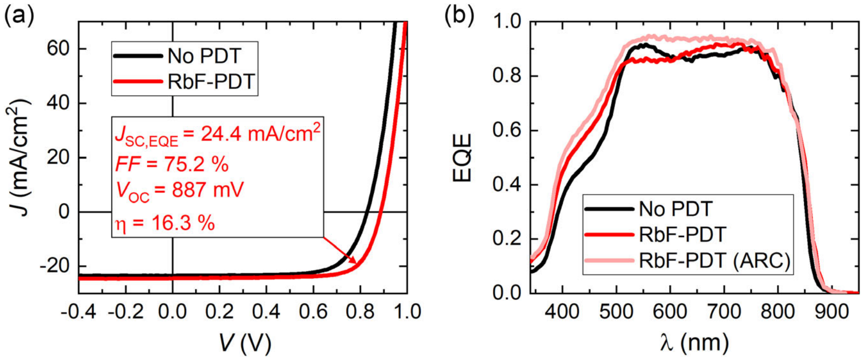

Figure 2. a) *I–V* and b) EQE characteristics of solar cells with similar, close-stoichiometric ACIGS composition without (black lines) and with (red lines) an applied RbF-PDT. The EQE spectrum of the RbF-PDT sample after deposition of an antireflection coating is shown as well.

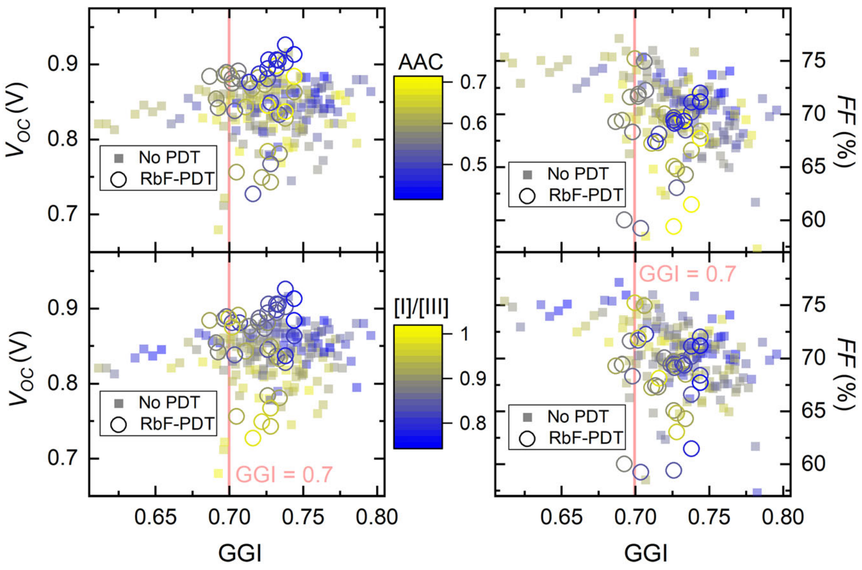

Figure 3. Open-circuit voltage (left) and FF (right) as a function of the GGI values for samples without (squares) and with (open circles) RbF-PDT. The color code illustrates the corresponding AAC (upper row) and [I]/[III] (lower row) values.

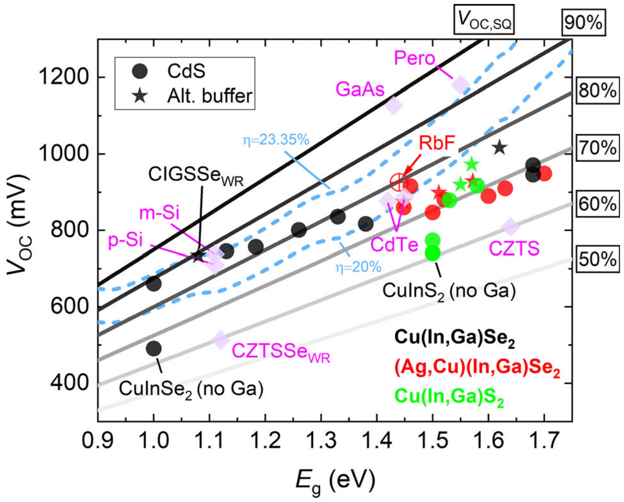

Figure 4. Highest V_{OC} values reported for chalcogenide-based solar cells as a function of E_g. The dots represent cells with CdS (best V_{OC} from this study marked "RbF") and the stars cells with alternative buffers. The best values for different other technologies are added as well.[4–9,28,29,31,60,64–77] The blue dashed lines show the V_{OC} values needed to reach efficiencies of 20% and 23.35%, assuming the same relative losses in FF and J_{SC} as reached for the chalcopyrite-based world record cell, i.e., 7% and 11%, respectively.

CdS when a clearly negative CBO is formed at the CdS/absorber interface ($E_g > 1.4$ eV for CIGS). However, even when using alternative buffers, the relative V_{OC} loss with respect to the radiative limit ($V_{OC,SQ}$) is always > 20% for $E_g > 1.3$ eV. This is far below the values for the best low-gap chalcopyrite ($V_{OC} \approx 0.90\ V_{OC,SQ}$) as well as GaAs and perovskite solar cells ($V_{OC} > 0.93\ V_{OC,SQ}$). This great gap is most likely caused by a lower "bulk lifetime" in wide-gap chalcopyrite devices and not an interface issue, as long as alternative buffers are used or sufficient Ag is alloyed to CIGS. The highest V_{OC} from this work reaches 80% of $V_{OC,SQ}$, which is, to the best of our knowledge, the by far highest value reported in this bandgap region (the data point next to it stems from our previous work on ACIGS without RbF-PDT[11]). This highlights the benefit of combining Ag-alloying and a heavy alkali PDT for wide-gap CIGS solar cells.

The blue dashed lines in Figure 4 show the V_{OC} values needed to reach efficiencies of 20% and 23.35% (world record), assuming the same relative losses (compared to the radiative limit) in FF and J_{SC} as reached for the world record cell, i.e., 7% and 11%, respectively.[4] Thus, if similarly low FF and J_{SC} losses could have been maintained, the sample with the highest V_{OC} from this work would have reached an efficiency > 21%. This shows that the rather low V_{OC} value is not the only bottleneck for wide-gap chalcopyrite solar cells; the transmittance of the buffer/window layer and the diffusion length need to be increased, too.

2.2. Material Characterization

This section presents the impact of the RbF-PDT on the ACIGS layer and its interfaces. It is divided into two parts. First, the surface modifications upon RbF-PDT are illustrated and in the second part the Rb distribution underneath the absorber surface is analyzed.

2.2.1. Absorber Surface Modifications upon RbF-PDT

Figure 5 shows scanning electron microscopy (SEM) images of the ACIGS surfaces from samples with (GGI = 0.71, AAC = 0.47, [I]/[III] = 0.85) and without (GGI = 0.73, AAC = 0.49, [I]/[III] = 0.85) RbF-PDT, before and after rinsing in deionized water for 60 s. The very similar absorber composition allows for a direct comparison of the surface morphology and corresponding modifications by the RbF-PDT. The water

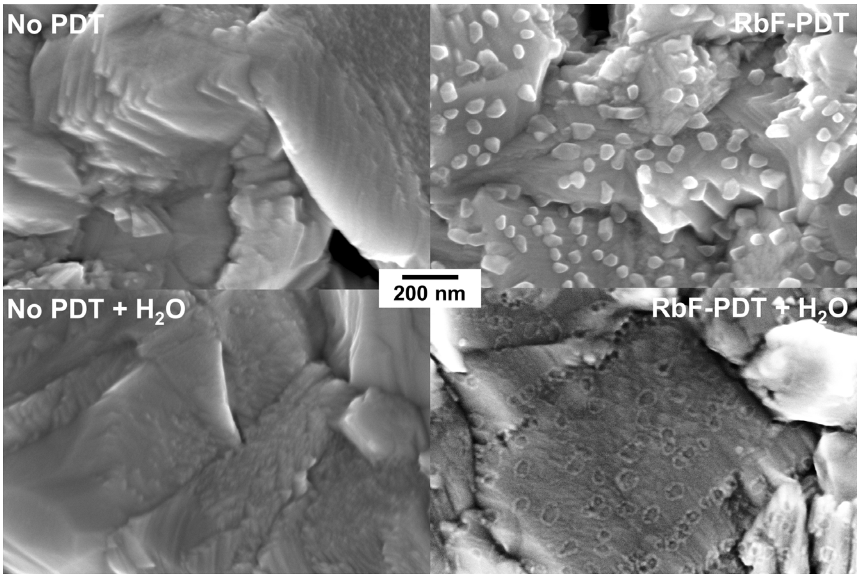

Figure 5. SEM images of the ACIGS surfaces without RbF-PDT (left) and with RbF-PDT (right), before and after water rinsing.

rinse mimics the situation during the initial phase of the CdS-CBD, when water-soluble phases are dissolved in the NH_3 solution.[44,78] Thus, the morphology and chemical properties of the H_2O-rinsed absorber surfaces are presumably very similar in the final device (i.e., after CdS deposition).

As frequently observed after a heavy alkali PDT of low-gap CIGS films,[42,44,53,61] also the surface of the Ag- and Ga-rich ACIGS layer is covered by homogenously distributed particles (≈40 nm diameter) after RbF-PDT (for lower magnification, see Figure S2, Supporting Information). These particles are not present without PDT. The water rinse removes all (most likely water-soluble) particles and leaves behind a very thin layer with openings where the particles were removed. Judging from the contrast of the SEM image, the layer is estimated to be at most a few nanometers thick.

In order to investigate modifications in surface chemistry by the RbF-PDT, the same bare absorber samples as presented in Figure 5 were analyzed by X-ray photoelectron spectroscopy (XPS). This allows determining chemical changes in the uppermost ≈5 nm of the films. The results are summarized in **Figure 6** and the corresponding changes in peak intensity are provided in Figure S3 in the Supporting Information.

After water rinsing, both samples show higher intensities for all elements except Na, Rb, and F. This is probably due to the dissolution of Na-containing compounds from the surface (see lower Na 1*s* peak intensity) because even the sample without RbF-PDT exhibits higher intensities of the absorber elements after rinsing. The Na 1*s* peak position indicates that these compounds are Na_2SeO_3 or NaOH, which are soluble in H_2O.[79] The Na 1*s* spectrum of the sample with RbF-PDT shows a shoulder toward lower binding energies (E_b) before water rinsing. This may suggest the formation of NaF or Na_2O upon RbF-PDT. The RbF-PDT sample initially shows a distinct F 1*s* signal, which vanishes after water rinsing. This correlates with the complete removal of the particles at the surface. In addition, the Rb 3*d* signal decreases and the shoulder in the Ga 3*d* peak ($E_b \approx 21$ eV), indicating the formation of an *x*-Ga–F (*x*: Rb or/and O, C, H, see following discussion) or Ga_xO compound, vanishes. In order to identify the chemical nature of the particles, energy-dispersive X-ray (EDX) analysis was conducted on the same sample (RbF-PDT before rinsing). Due to a small but unavoidable sample drift in SEM, only bigger particles (or agglomerates) could be analyzed reliably. It is evident that the Ga and Rb concentrations are significantly increased at positions where particles are present (see Figure S4 in Supporting Information). Thus, it is proposed that the particles forming upon RbF-PDT are Rb–Ga–F compounds. Possible candidates are, e.g., Rb_3GaF_6, $RbGaF_4$, or $RbGa_2F_7$.[80] However, it cannot be excluded that the analyzed particles are in fact agglomerates of smaller binary particles, e.g., GaF_3 and RbF lumped together. The EDX analysis further suggests that most particles are also enriched in oxygen (Figure S4, Supporting Information), so even the formation of multinary oxides cannot be excluded. Similar to NaF,[81,82] the presence of RbF may, for instance, catalyze Ga_xO formation at the surface. However, the oxide formation may also have taken place during air exposure of the samples (i.e., preferential oxidation of particles). In each case, the ACIGS surface should consequently be depleted in Ga after water rinsing or CdS deposition.

The In signal slightly increases after RbF-PDT, while all other metal elements are substantially reduced. This indicates the formation of an Rb-containing surface layer (compare Figure 5), which has a lower Ag, Cu, and Ga concentration than the underlying absorber material. Considering the Rb 3*d* peak positions, this layer may well be $RbInSe_2$, as proposed earlier for CIGS after RbF-PDT and as measured on an $RbInSe_2$ reference layer.[83] However, also the Se 4*d* intensity is reduced after PDT, which is not understood at this stage. A possible scenario may be that the RbF-PDT step removes Se-containing phases from the surface, e.g., due to the difference in the temperature profile after absorber deposition.

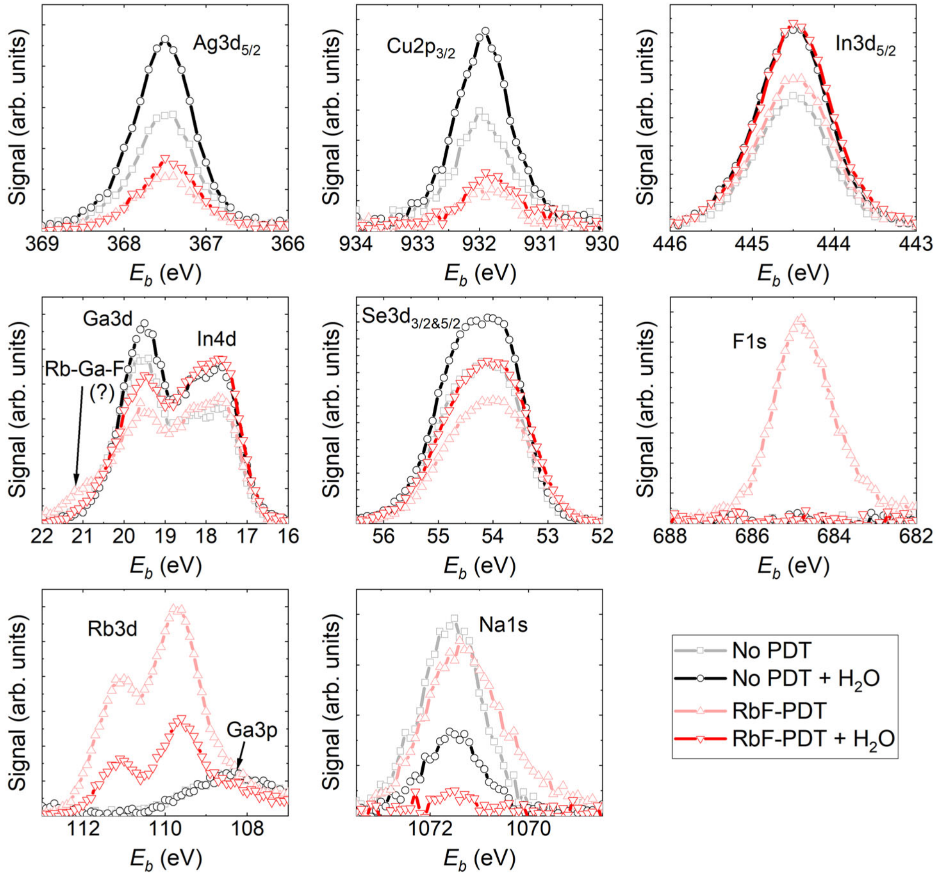

Figure 6. Binding energies of selective core level electrons for the absorber elements as well as for Rb, Na, and F, as deduced from XPS measurements. The ACIGS samples, with and without RbF-PDT and water rinsing, are the same as presented in Figure 5 and have roughly the same integral composition.

The formation of a very thin $RbInSe_2$ surface layer (<5 nm) is also suggested in other studies from experimental nanoscale analysis of the CdS/CIGS interface via atom probe tomography (APT) and high-resolution transmission electron microscopy (TEM).[47,61,84] However, it is still under debate if this layer always forms and whether it is covering the whole surface or not.[85]

Figure 7a shows a scanning TEM (STEM) high-angle annular dark field (HAADF) image of the heterojunction region in the best ACIGS solar cell sample with RbF-PDT ($\eta = 16.3\%$, see Figure 2a) that has a composition of GGI = 0.70, AAC = 0.61, and [I]/[III] = 0.96. In the center, the Rb concentration map, as derived from EDX analysis, is superimposed. A very confined agglomeration of Rb at the buffer/absorber interface is evident.

In Figure 7b, the Cd, Rb, and Ag maps are superimposed with the STEM image. The Rb signal can be clearly spatially separated from the Cd and Ag signals, suggesting the existence of a separate Rb-containing layer. Figure 7c illustrates the quantified and normalized elemental line profiles across the heterojunction. The analyzed line/rectangle is indicated by the white arrow in Figure 7b. At the position where the Rb signal peaks, all absorber elements except indium already dropped (at a distance of ≈5 nm). This may indicate the presence of an $RbInSe_2$ layer as already suggested by the XPS results. However, the same controversy as observed in XPS analysis is seen in STEM-EDX, namely, that the normalized Se signal drops at the same position as Ag and Cu. At this point this cannot be explained, but a possible reason may be that the atomic concentration of In would increase significantly from the ACIGS to the $RbInSe_2$ layer (about threefold), while the Se signal would stay the same. The very small extension of the potential $RbInSe_2$ layer makes its identification additionally challenging. Even in high-resolution STEM analysis, no interlayer between the ACIGS and CdS could be found (see Figure S5, Supporting Information).

It is noteworthy that the Ga signal drops about 15 nm before the indium signal. This feature was observed at several additional positions that were analyzed (see Figure S6, Supporting Information), showing a gradual decrease in GGI about 10–50 nm underneath the CdS layer. A possible reason could be the Rb–Ga–F, GaF_3 or Ga_xO formation during RbF-PDT that depletes the surface of Ga.

Despite some controversy and without providing a final proof, we deem it likely that the RbF-PDT creates an $RbInSe_2$ layer with openings at the surface of the ACIGS film. However, it is still under debate if such a layer is beneficial for the device performance or not. It was, for instance, reported that an RbF- and CsF-PDT result in similarly improved electrical characteristics (including efficiency) of CIGS solar cells, while an Alkali–In–Se_2 surface layer was only found after RbF- and not after CsF-

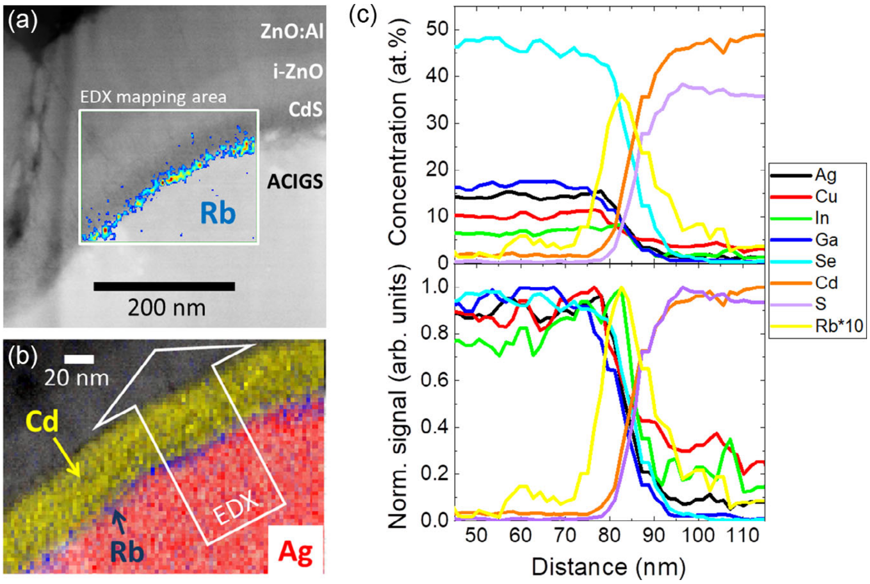

Figure 7. a) STEM HAADF image of the heterojunction region in the champion device subjected to an RbF-PDT (compare Figure 2). The Rb concentration map, deduced from EDX, is superimposed. b) Overlay of the Cd, Rb, and Ag signals in the corresponding EDX mapping area. c) Absolute and normalized elemental concentration profiles across the heterojunction (location indicated by arrow in (b)).

PDT.[48] Other studies observed the formation of $CsInSe_2$ surface patches after a highly dosed CsF-PDT,[86] while the coverage/morphology of the Alkali–In–Se_2 phase may be affected by oxygen exposure prior to the PDT.[87] In addition, a selective removal of the Alkali–In–Se_2 top layer by an HCl etch was found to reverse the beneficial effects of a heavy-alkali PDT, while a subsequent annealing step (i.e., redistribution of the alkali atoms) can restore most of the V_{OC} gain again.[78,88] These findings rather indicate that the formation of an Alkali–In–Se_2 layer is not the main factor explaining the beneficial effect of the heavy-alkali PDT. The presence of a "too thick" $RbInSe_2$ layer and/or too little exposed ACIGS surface area after particle dissolution during CBD (i.e., too few/small particles formed during PDT) may explain why the FF tends to be lower for samples subjected to an RbF-PDT. Especially for ACIGS with high Ag contents (high electron affinity) a high conduction band offset is expected between the absorber and a wide-gap Alkali–In–Se_2 layer,[46,89,90] which would result in a transport barrier for electrons.[43,86,91,92] But as mentioned above, it cannot be excluded that the RbF-PDT of wide-gap ACIGS leads to a slightly different surface modification as usually reported for standard CIGS absorbers and discussing the effect of a potentially absent $RbInSe_2$ layer (see "Se controversy") may be needless.

2.2.2. Rubidium Incorporation Underneath Absorber Surface

To investigate the Rb distribution in the absorber bulk and at the back contact, glow-discharge optical emission spectroscopy (GDOES) was employed on the exact same bare absorber samples analyzed by SEM and XPS. **Figure 8** shows the corresponding nonquantified depth profiles of Rb, Na, Cu, and Mo. As orientations, the onset of the Mo signal (black dashed line) and the Na level in the bulk (red dashed line) is indicated. A more detailed view of the interface regions can be found in Figure S7 in the Supporting Information.

In both samples, the water rinse lowers the amount of alkali atoms at the surface, in agreement with the XPS results. Underneath the very surface, the Na content is still higher than in the bulk even after the dissolution of Na-containing compounds. This is due to the agglomeration of Na in the OVCs at the surface,[31] leading to stoichiometry-dependent Na depth profiles in ACIGS films (see Figure S8 in Supporting Information). After the PDT, Rb is mainly present not only at the interfaces, but also in the bulk of the absorber and probably in the GBs of the Mo electrode. The signal from the bulk region originates almost exclusively from the Rb decoration of random high-angle GBs.[85,87,93,94] While heavier alkali elements can easily substitute Na in GBs, their diffusion into the grain interior is hindered when the group-I vacancies are already occupied by Na,[95] as it is the case in this study. It is still surprising that the bulk (i.e., grain interior plus GBs) level of sodium is only marginally reduced after PDT. A possible explanation is the relatively large Na solubility in ACIGS with high Ag contents,[96] so that the measured bulk level is mainly governed by Na in the absorber lattice. It was suggested before that the alkali exchange in the GBs leads to an in-diffusion of Na into the grain interior.[50,97]

The rinsing reduces the Rb signal at the surface (i.e., removal of Rb–Ga–F or RbF) and also slightly in the bulk. The latter observation is presumably a result of Rb diffusion toward the surface and subsequent removal upon rinsing. As previously observed for low-gap chalcopyrite absorbers,[56,69] the heavier alkali element substitutes Na at the $MoSe_2$/absorber interface (compare onset of Mo signal). This process is suggested to cause a larger back contact barrier and may be the reason for the trend of lower FF values after RbF-PDT.[56,98]

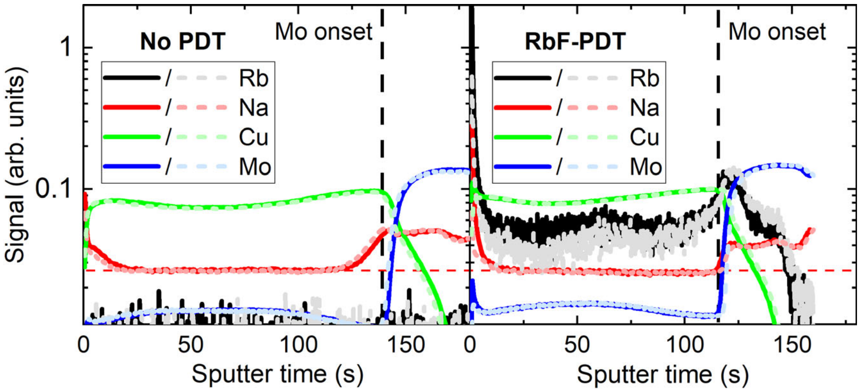

Figure 8. Elemental depth profiles of Rb, Na, Cu, and Mo as measured by GDOES on bare absorber samples without (left, GGI = 0.71, AAC = 0.47, [I]/[III] = 0.85) and with RbF-PDT (right, GGI = 0.73, AAC = 0.49, [I]/[III] = 0.85). The solid lines represent the samples before and the pale, dashed lines after water rinsing.

To investigate the overall Rb distribution in an ACIGS solar cell with OVCs at the surface, a more off-stoichiometric sample than presented in Figure 7 was analyzed by STEM-EDX. **Figure 9**a shows the corresponding cross section of a solar cell subjected to an RbF-PDT with an ACIGS composition of GGI = 0.70, AAC = 0.56, and [I]/[III] = 0.86. The bright spheres are pure Ag droplets, forming during preparation and observation (i.e., electron exposure) of the TEM lamella, similar to the Cu precipitates found on CIGS TEM lamellae.[99] An OVC patch is clearly visible in the upper right corner. The elemental maps presented in Figure 9b reveal that the OVC is significantly depleted in Ag and enriched in Ga. Rubidium is only detected (above the noise level) at the interfaces and in certain GBs. It appears that Rb is continuously present at the CdS/ACIGS interface across the whole lamella width, in line with the proposed formation of an $RbInSe_2$ layer. Figure 9c shows a line profile across the whole absorber depth (position illustrated in Figure 9b). The GGI grading toward the back contact is accompanied by a reduction in Ag content. This behavior was observed earlier and suggested to be a consequence of a miscibility gap.[7,100,101]

Figure 10a shows a higher magnified bright field STEM image of the region containing the OVC patch seen in Figure 9. The corresponding EDX mappings of the absorber elements and Rb are presented in Figure 10b. Rubidium is mainly found in the GB and at the interface to the buffer. No clear difference between the Rb concentration at the CdS/ACIGS and at the CdS/OVC interface can be determined. If the hypothesis is true that the Rb signal at the buffer interface stems from an $RbInSe_2$ layer, its growth/formation would not be significantly different on ACIGS as compared to on an OVC surface. Furthermore, there is no clear indication of an Rb agglomeration inside the OVC phase. In order to quantify phase-dependent elemental changes, a line profile across the ACIGS/OVC/CdS interfaces (arrow in Figure 10b) was extracted. The results are presented in Figure 10c. It is obvious that the absorber stoichiometry abruptly changes from 1:1:2 to 1:3:5 at the ACIGS/OVC interface. The

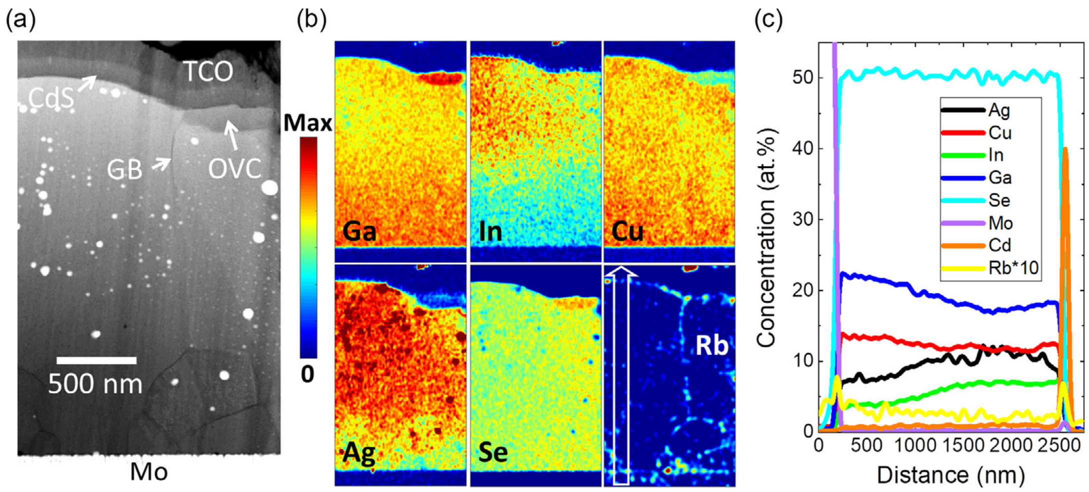

Figure 9. a) STEM HAADF image of a solar cell cross section with an off-stoichiometric ACIGS absorber (GGI = 0.70, AAC = 0.56, and [I]/[III] = 0.86) subjected to an RbF-PDT. The nanosized spheres (bright dots) are Ag precipitates. b) Corresponding elemental maps and c) line profile along the white arrow in (b), as deduced from STEM-EDX.

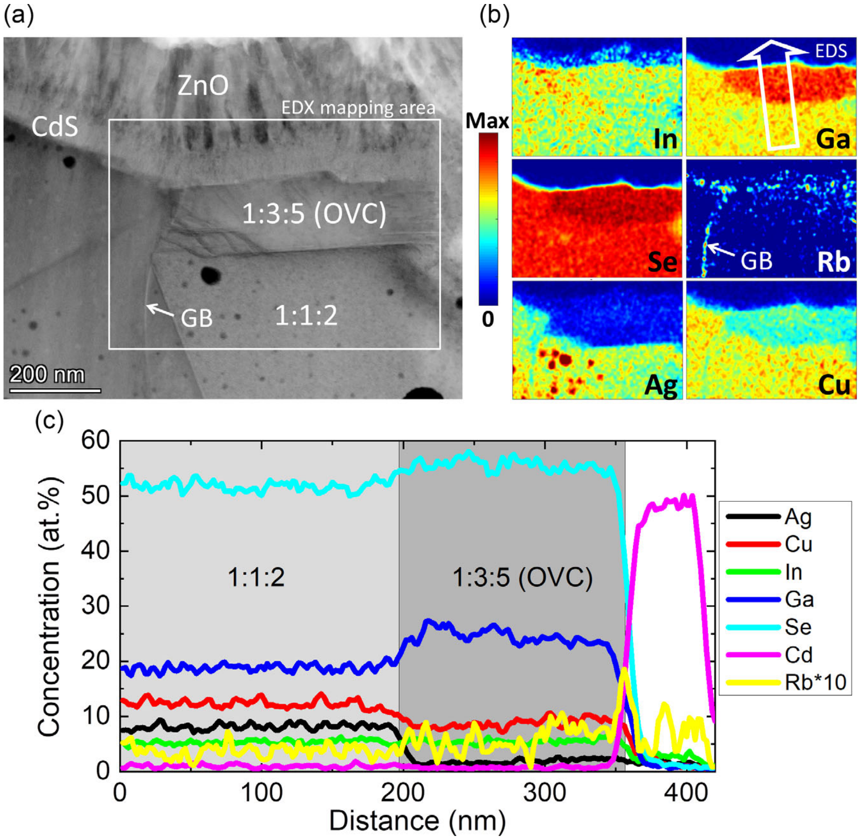

Figure 10. More detailed analysis of the heterojunction region of the same sample presented in Figure 8 (GGI = 0.70, AAC = 0.56, and [I]/[III] = 0.86 with RbF-PDT). a) STEM bright field image, b) elemental mappings, and c) line profile across the 1:1:2/OVC/CdS interfaces as deduced from STEM-EDX.

reduction in group-I concentration is mainly governed by a strong decrease in Ag content. The rubidium signal shows a peak at the OVC/CdS interface, but no clear increase in the OVC as compared to the 1:1:2 phase (i.e., presumably noise level) is found. However, differences at such small atomic concentrations ($c_{Rb} \leq 0.5$ at%) are challenging to quantify via STEM-EDX.

It was found that OVCs in ACIGS strongly accumulate Na (see again Figure S8, Supporting Information).[31] The Na occupation of group-I vacancies in the OVCs and the degree of alkali saturation very likely affect the potential incorporation of Rb into the OVCs. In order to quantify the Na concentration within the OVCs before RbF-PDT, APT was conducted on an ACIGS absorber with a high off-stoichiometry of [I]/[III] = 0.76. In addition, a high AAC = 0.80 and GGI = 0.85 was chosen for this sample to increase the OVC volume fraction[11,31] and thereby the chances to extract an APT tip that contains a 1:1:2/1:3:5 phase boundary. **Figure 11**a shows the corresponding sample reconstruction for Cu and Na. The ACIGS/OVC interface is located in the upper part of the tip (i.e., up to ≈100 nm below the CdS layer). Obviously, the OVC strongly accumulates Na. The atomic concentrations as well as the AAC, GGI, and [I]/[III] ratios across 1:1:2/1:3:5 interface are presented in Figure 11b,c. Similar to the STEM-EDX results in Figure 10 (different samples), the AAC is significantly reduced in the OVC and the composition matches a 1:3:5 stoichiometry. Sodium accumulates at the OVC/1:1:2 interface (similarly as in GBs), but even in the OVC bulk a significant Na content of $c_{Na} \approx 0.3$–0.4 at% is measured. Assuming that the OVCs are saturated in Na, this number may roughly represent the upper limit for alkali incorporation. As the noise level of the Rb signal in STEM-EDX is in a similar range, it cannot be excluded that Rb is still incorporated into the OVCs upon RbF-PDT. Indeed, ATP results from Stokes et al. suggest potassium enrichment in OVCs at the CIGS surface after KF-PDT, although Na was provided during growth.[102] However, a comparison of Na depth-profiles in off-stoichiometric ACIGS without and with RbF-PDT via GDOES shows no indication that the Na content in the OVCs is reduced after the RbF-PDT in this study (not shown here). Thus, the presence of sodium in the OVC lattice presumably impedes in-diffusion/replacement of/by rubidium, similarly as was reported for the chalcopyrite 1:1:2 phase before.[95]

To conclude, it is proposed that the presence of OVCs (very abundant in ACIGS with high Ag contents) does not significantly affect the incorporation and distribution of Rb upon PDT, as long as Na was introduced before. For the future, further APT measurements on ACIGS films subjected to an RbF-PDT are planned to analyze the Rb and Na distribution in the OVCs and confirm this hypothesis.

Finally, a closer look on the GB chemistry in RbF-treated ACIGS shall be provided. The elemental maps of the off-stoichiometric ([I]/[III] = 0.86) sample in Figure 10b indicate compositional changes at the GB. This particular GB shows a

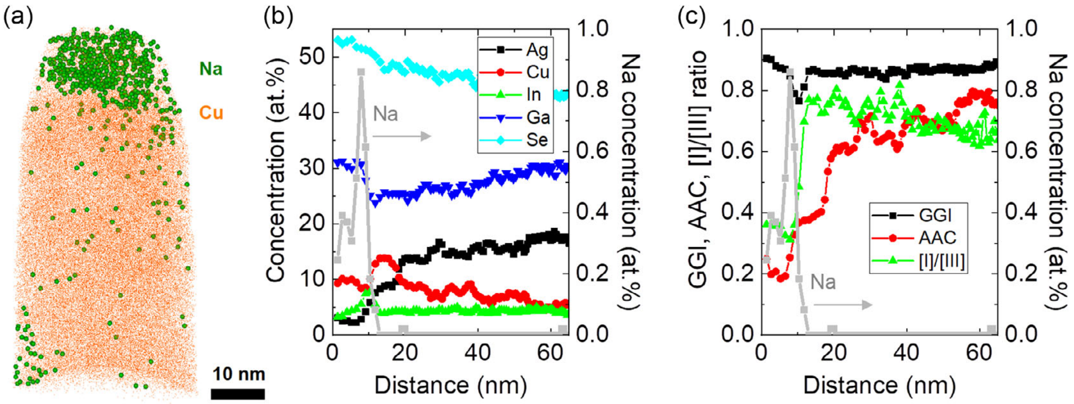

Figure 11. a) Sample tip reconstruction (only Cu and Na shown) of a sample without RbF-PDT (GGI = 0.85, AAC = 0.80, and [I]/[III] = 0.76), as deduced by APT. b) Corresponding elemental line profile and c) GGI, AAC, and [I]/[III] ratios across the OVC/1:1:2 interface located at the top of the tip.

reduction in both group-I elements, accompanying the Rb decoration. A corresponding elemental line profile can be found in Figure S9 in Supporting Information, confirming that the GB is indeed depleted in Ag and Cu. In order to obtain more statistical significance, the back contact region of the same sample, which contains smaller grains (more GBs), was investigated in more detail. The results of the corresponding STEM-EDX analysis are illustrated in **Figure 12**. Apart from a clear Rb accumulation, most observed GBs show a relatively pronounced group-I depletion. This also becomes evident in the [I]/[III] ratio map. Again, corresponding line profiles (exemplified in Figure S10, Supporting Information) reveal that the GBs are depleted in both group-I elements. This is in line with other studies, reporting on a slightly more pronounced (or frequent) group-I depletion in CIGS GBs after heavy alkali PDT,[50,84,103] which is claimed to make them electrically benign.[21] Thus, it may be suggested that a lower recombination rate at GBs is responsible for the V_{OC} increase for the RbF-treated samples. However, no chemical changes were found in GBs of the best sample made in this study ($\eta = 16.3\%$), as can be seen in Figure S11 and S12 in the Supporting Information. In contrast to the absorber in Figure 12, this sample has a very close-stoichiometric ACIGS composition of [I]/[III] = 0.96. This observation makes it unlikely that a potential group-I depletion in the GBs causes the beneficial effect of the RbF-PDT. It is rather suggested that the integral absorber off-stoichiometry is partly accounted for by a group-I depletion in the GBs. Consequently, (close-) stoichiometric absorbers would show less or no chemical change in the GBs, independent of the incorporation of heavy alkali elements.

In summary, the extensive material characterization reveals that the heavy alkali PDT of wide-gap ACIGS absorbers has very similar effects as compared to “standard” low-gap CIGS films. A continuous accumulation of Rb is found at all interfaces (including high-angle random GBs). On the other hand, the diffusion of

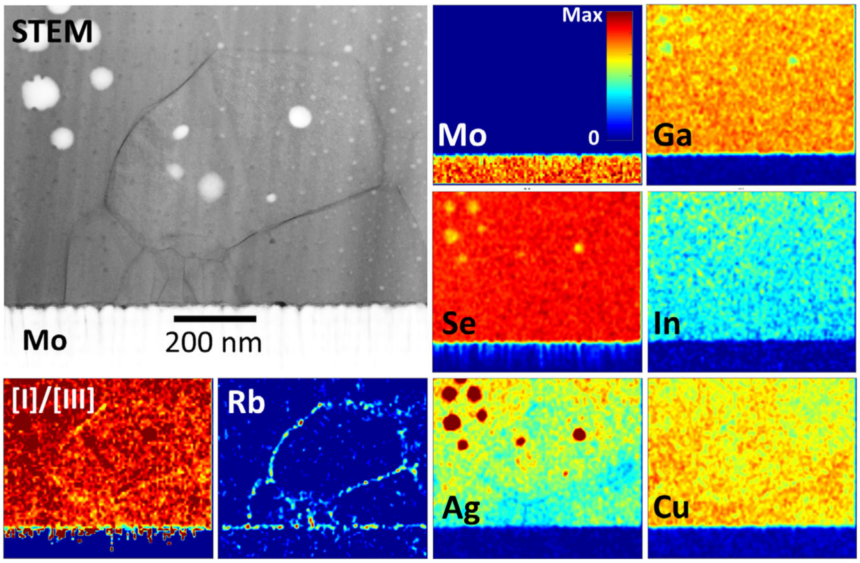

Figure 12. More detailed analysis of the back contact region and corresponding GBs of the same sample presented in Figure 8 and 9 (GGI = 0.70, AAC = 0.56, and [I]/[III] = 0.86 with RbF-PDT). STEM HAADF image (upper left corner) and elemental mappings as deduced from STEM-EDX.

Rb into the chalcopyrite and OVC absorber lattice is deemed unlikely or at least very limited. Surface analysis indicates the formation of a Ag-, Cu-, and Ga-depleted surface phase, containing openings after water rinsing and most likely also in the final solar cell structure (i.e., after CBD of CdS). It is proposed that this layer is $RbInSe_2$, but no final evidence could be provided. Finally, group-I depleted GBs were found for an off-stoichiometric absorber after RbF-PDT, but not for a stoichiometric one. Overall, similar to the case of low-gap CIGS solar cells, it cannot be concluded which effect it is that leads to the higher V_{OC} for wide-gap ACIGS samples subjected to a heavy alkali PDT.

3. Conclusions

The impact of an RbF-PDT on wide-gap ACIGS films and corresponding solar cells is investigated. Little to no effect on absorber doping is observed. Consequently, the previously revealed (doping related) anticorrelation between J_{SC} and V_{OC} with varying ACIGS stoichiometry for nontreated absorbers is also found for RbF-treated samples. On average, higher V_{OC} and J_{SC}, but lower FF values were measured when the absorber was subjected to the PDT. Consequently, no clear efficiency increase is evident for the majority of cells. However, for two individual (close-stoichiometric) samples the FF drop could be avoided, while the boost in V_{OC} and J_{SC} after RbF-PDT is maintained. As a result, efficiencies up to 16.3% (no ARC) at $E_g = 1.43$ eV were reached. A record V_{OC} value of 926 mV at $E_g = 1.44$ eV (i.e., ≈80% of radiative limit) was measured on a sample with a large off-stoichiometry of [I]/[III] = 0.80. It is suggested that lower V_{OC} deficits require a substantial improvement in absorber bulk quality, like the passivation/reduction of deep defects.

Extensive material characterization revealed that the RbF-PDT results in very similar absorber modifications for wide-gap ACIGS as previously reported for "standard" low-gap CIGS absorbers. Rubidium is incorporated continuously alongside all absorber interfaces, including random high angle GBs. It is not clear though if it always induces beneficial chemical changes (e.g., group-I depletion) in GBs. The diffusion into the absorber bulk (1:1:2 and 1:3:5) is deemed very limited, but further analysis is needed for confirmation. Surface analysis further indicates the formation of a very thin Rb-containing layer on top of ACIGS after RbF-PDT that is proposed (but not unambiguously proven) to be $RbInSe_2$. The diversity of possible origins makes it challenging to identify the effects causing the boost in V_{OC} (and drop in FF) after RbF-PDT.

4. Experimental Section

Solar Cell Processing: A stack of soda lime glass (SLG)/Mo/NaF/ACIGS/CdS/i-ZnO/ZnO:Al was used for all solar cell samples in this study. First, a Mo back contact was sputtered (DC) on SLG substrates, followed by the evaporation of 10–15 nm-thick NaF. Sodium in-diffusion from the SLG was allowed (no alkali diffusion-barrier was used). A three-stage (I-poor → I-rich → I-poor) coevaporation process was applied to grow 2.0–2.4 µm-thick ACIGS films at a maximum temperature of 550 °C. During absorber deposition, the ratio of the Ag and Cu evaporation rates was kept constant at any time. Higher Ga and lower In rates in the initial growth stages led to the formation of a bandgap grading toward the back contact. The compositional (GGI and AAC) grading was not intentionally varied in this study. After absorber deposition, the metal sources were switched off and an RbF-PDT was applied at $T \approx 350$ °C for about 15 min at a rate of ≈1 nm min^{-1} in Se-containing atmosphere. In total, 13 ACIGS depositions were done, resulting in 44 individual samples with unique compositions in the range of AAC = 0.46–0.71, GGI = 0.69–0.74, and [I]/[III] = 0.77–0.98. Differences in composition emanate from lateral distribution of the metal sources in the evaporation chamber. The integral compositions were deduced from cross-calibrated X-ray fluorescence measurements on bare absorbers. For further information on the deposition protocol and compositional spreads, we refer to the study by Keller et al.[11] Subsequently, a 44 nm-thick CdS buffer layer was grown for 4 min in a preheated (60 °C) chemical bath (the samples without RbF-PDT from our previous study had 57 nm CdS). Finally, a window layer stack consisting of i-ZnO (60 nm) and ZnO:Al (200 nm; sheet resistance ≈50 Ω sq^{-1}) was sputtered on top. Only for the best solar cell sample, a ≈ 105 nm-thick MgF_2 ARC was deposited on the ZnO:Al. In the final step, the samples were sectioned into 14 individual solar cells ($A = 0.05$ cm^2) by mechanical scribing.

Material Characterization: GDOES was conducted in a Spectruma Analytik GDA 750HR system to measure nonquantified elemental depth profiles.

A Zeiss Merlin scanning electron microscope was used ($V_{acc} = 5$ kV) to investigate the absorber surfaces before and after water rinsing and RbF-PDT. STEM and EDX analyses were performed on a FEI Titan Themis XFEG instrument equipped with a super-*x* detector and operated at 200 kV. The TEM lamellae were prepared via focused ion beam in a Crossbeam 550 FEI system, following the lift-out technique. A final milling step at maximum 5 kV ion accelerating voltage was performed on both sides of the lamellae, and no further electron exposure was done in the FIB before the TEM analyses.

Chemical modifications after the RbF-PDT were measured in a Quantera II Scanning XPS Microprobe system (Physical Electronics), using monochromatic Al Kα (1.487 keV) X-ray radiation and charge compensation. The sodium concentration in an OVC patch (before RbF-PDT) was examined via APT analysis. A dual-beam focused ion-beam/scanning electron microscope instrument (Thermo-Fisher Versa 3D) was used to prepare the needle-shaped tip for APT. A 100 nm-thick Pt layer was deposited beforehand and an acceleration voltage of 2 kV was applied in the final steps of tip shaping to minimize Ga implantation. In addition, electron-beam exposure during preparation was minimized to prevent segregation of Ag precipitates on the tip's surface.[32,99] Laser-pulsed APT measurements were carried out in a LEAP 3000X HR CAMECA system using a green laser ($\lambda = 532$ nm) with a laser power set to 0.05 nJ, a repetition rate of 100 kHz, and base temperature of ≈50 K. 3D reconstructions and data analysis were performed using CAMECA IVAS 3.6.14 software.

Integral absorber film compositions were determined with the XRF spectrometer Epsilon 5 (Panalytical).

Electro-Optical Characterization of Solar Cells: The EQE (only best cell each) and *I–V* (all 14 cells per sample) measurements of completed solar cells were conducted in home-built setups. The *I–V* characteristics were deduced at $T = 25$ °C and under illumination by an ELH lamp. For each sample, the light intensity was calibrated to match the $J_{SC,EQE}$ value, as calculated from the corresponding EQE spectra for illumination with the AM1.5G spectrum. The space charge region width of selective samples was determined by *C–V* profiling, sweeping the voltage from $V = -0.5$ to 0.7 V with a probing frequency of 60 kHz and an amplitude of 25 mV. A dielectric constant of $\varepsilon_r = 10$ was assumed.

Supporting Information

Supporting Information is available from the Wiley Online Library or from the author.

Acknowledgements

This work was supported by the Swedish Foundation for Strategic Research (SSF) under the project number RMA15-0030 and by the Swedish Energy

Agency under the project number P50992-1, Dnr 2020-009335. Olof Stolt and Nina Shariati-Nilsson are gratefully acknowledged for helping to prepare and measure the solar cell samples. The authors also thank Patrick Pearson for conducting capacitance profiling measurements.

Conflict of Interest

The authors declare no conflict of interest.

Data Availability Statement

Research data are not shared.

Keywords

(Ag,Cu)(In,Ga)Se_2 (ACIGS), Cu(In,Ga)Se_2 (CIGS), RbF postdeposition treatment (RbF-PDT), stoichiometry, wide-gap chalcopyrite

Received: January 14, 2022
Revised: February 3, 2022

---

[1] A. S. Brown, M. A. Green, *Phys. E* **2002**, *14*, 96.
[2] R. K. Kothandaraman, Y. Jiang, T. Feurer, A. N. Tiwari, F. Fu, *Small Methods* **2020**, *4*, 2000395.
[3] P. Jackson, R. Wuerz, D. Hariskos, E. Lotter, W. Witte, M. Powalla, *Phys. Status Solidi RRL* **2016**, *586*, 583.
[4] M. Nakamura, K. Yamaguchi, Y. Kimoto, Y. Yasaki, T. Kato, H. Sugimoto, *IEEE J. Photovoltaics* **2019**, *9*, 1863.
[5] M. A. Contreras, L. M. Mansfield, B. Egaas, J. Li, M. Romero, R. Noufi, E. Rudiger-Voigt, W. Mannstadt, *Prog. Photovolt. Res. Appl.* **2012**, *20*, 843.
[6] F. Larsson, N. S. Nilsson, J. Keller, C. Frisk, V. Kosyak, M. Edoff, T. Törndahl, *Prog. Photovolt. Res. Appl.* **2017**, *25*, 755.
[7] J. Keller, K. V. Sopiha, O. Stolt, L. Stolt, C. Persson, J. J. S. Scragg, T. Törndahl, M. Edoff, *Prog. Photovolt. Res. Appl.* **2020**, *28*, 237.
[8] H. Hiroi, Y. Iwata, S. Adachi, H. Sugimoto, A. Yamada, *IEEE J. Photovoltaics* **2016**, *6*, 760.
[9] H. Hiroi, Y. Iwata, H. Sugimoto, A. Yamada, *IEEE J. Photovoltaics* **2016**, *6*, 1630.
[10] J. Lindahl, J. Keller, O. Donzel-Gargand, P. Szaniawski, M. Edoff, T. Törndahl, *Sol. Energy Mater. Sol. Cells* **2016**, *144*, 684.
[11] J. Keller, P. Pearson, N. Shariati Nilsson, O. Stolt, L. Stolt, M. Edoff, *Sol. RRL* **2021**, *5*, 2100403.
[12] S. Siebentritt, U. Rau, *Wide-Gap Chalcopyrites*, Springer-Verlag, Berlin Heidelberg **2006**.
[13] B. Huang, S. Chen, H. Deng, L. Wang, M. A. Contreras, R. Noufi, S.-H. Wei, *IEEE J. Photovoltaics* **2014**, *4*, 477.
[14] J. Pohl, K. Albe, *Phys. Rev. B.* **2013**, *87*, 245203.
[15] C. Spindler, F. Babbe, M. H. Wolter, F. Ehre, K. Santosh, P. Hilgert, F. Werner, S. Siebentritt, *Phys. Rev. Mater.* **2019**, *3*, 090302.
[16] C. Spindler, D. Regesch, S. Siebentritt, *Appl. Phys. Lett.* **2016**, *109*, 032105.
[17] S. Lany, A. Zunger, *J. Appl. Phys.* **2006**, *100*, 113725.
[18] G. Hanna, A. Jasenek, U. Rau, H. W. Schock, *Thin Solid Films* **2001**, *387*, 71.
[19] G. Hanna, A. Jasenek, U. Rau, H. W. Schock, *Phys. Status Solidi A* **2000**, *179*, 73.
[20] M. R. Balboul, H. W. Schock, S. A. Fayak, A. A. El-Aal, J. H. Werner, A. A. Ramadan, *Appl. Phys. A* **2008**, *92*, 557.
[21] M. Raghuwanshi, R. Wuerz, O. Cojocaru-Mirédin, *Adv. Funct. Mater.* **2020**, *30*, 2001046.
[22] M. Raghuwanshi, E. Cadel, P. Pareige, S. Duguay, F. Couzinie-Devy, L. Arzel, N. Barreau, *Appl. Phys. Lett.* **2014**, *105*, 013902.
[23] S.-H. Wei, A. Zunger, *J. Appl. Phys.* **1995**, *78*, 3846.
[24] M. Gloeckler, J. R. Sites, *Thin Solid Films* **2005**, *480–481*, 241.
[25] M. Turcu, O. Pakma, U. Rau, *Appl. Phys. Lett.* **2002**, *80*, 2598.
[26] S. Chen, X. G. Gong, S. H. Wei, *Phys. Rev. B* **2007**, *75*, 205209.
[27] D. Huang, J. W. Jiang, J. Guo, Y. J. Zhao, R. Chen, C. Persson, *Mater. Sci. Eng., B* **2018**, *236–237*, 147.
[28] G. M. Hanket, J. H. Boyle, W. N. Shafarman, in *34th IEEE Photovolt. Spec. Conf.* **2009**, pp. 001240–001245, https://doi.org/10.1109/PVSC.2009.5411241.
[29] T. Nakada, K. Yamada, R. Arai, H. Ishizaki, N. Yamada, *MRS Proc.* **2005**, *865*, F11.1.
[30] T. Umehara, F. Zulkifly, K. Nakada, A. Yamada, *Jpn. J. Appl. Phys.* **2017**, *56*, 08MC09.
[31] J. Keller, L. Stolt, K. V. Sopiha, J. K. Larsen, L. Riekehr, M. Edoff, *Sol. RRL* **2020**, *4*, 2000508.
[32] J. K. Larsen, O. Donzel-Gargand, K. V. Sopiha, J. Keller, K. Lindgren, C. Platzer-Björkman, M. Edoff, *ACS Appl. Energy Mater.* **2021**, *4*, 1805.
[33] J. C. Mikkelsen, *Mater. Res. Bull.* **1977**, *12*, 497.
[34] H. Simchi, B. McCandless, W. Shafarman, K. Kim, J. Boyle, R. Birkmire, in *37th IEEE Photovolt. Spec. Conf.* **2011**, pp. 000041–000045, https://doi.org/10.1109/PVSC.2011.6185840.
[35] J. H. Boyle, B. E. McCandless, G. M. Hanket, W. N. Shafarman, *Thin Solid Films* **2011**, *519*, 7292.
[36] A. Chirila, P. Reinhard, F. Pianezzi, P. Blösch, A. R. Uhl, C. Fella, L. Kranz, D. Keller, C. Gretener, H. Hagendorfer, D. Jaeger, R. Erni, S. Nishiwaki, S. Buecheler, A. N. Tiwari, *Nat. Mater.* **2013**, *12*, 1107.
[37] P. Reinhard, B. Bissig, F. Pianezzi, E. Avancini, H. Hagendorfer, D. Keller, P. Fuchs, M. Döbeli, C. Vigo, P. Crivelli, S. Nishiwaki, S. Buecheler, A. N. Tiwari, *Chem. Mater.* **2015**, *27*, 5755.
[38] T. M. Friedlmeier, P. Jackson, D. Kreikemeyer-lorenzo, D. Hauschild, O. Kiowski, D. Hariskos, L. Weinhardt, C. Heske, M. Powalla, S.-W. B. Zsw, in *IEEE 43rd Photovolt. Spec. Conf. (PVSC)* **2016**, pp. 0457–0461, https://doi.org/10.1109/PVSC.2016.7749634.
[39] T. M. Friedlmeier, P. Jackson, A. Bauer, D. Hariskos, O. Kiowski, R. Wuerz, M. Powalla, *IEEE J. Photovoltaics* **2015**, *5*, 1487.
[40] T. Feurer, F. Fu, T. P. Weiss, E. Avancini, J. Löckinger, S. Buecheler, A. N. Tiwari, *Thin Solid Films* **2019**, *670*, 34.
[41] P. Reinhard, F. Pianezzi, B. Bissig, A. Chiril, P. Blösch, S. Nishiwaki, *IEEE J. Photovoltaics* **2015**, *5*, 656.
[42] T. Kodalle, M. D. Heinemann, D. Greiner, H. A. Yetkin, M. Klupsch, C. Li, P. A. van Aken, I. Lauermann, R. Schlatmann, C. A. Kaufmann, *Sol. RRL* **2018**, *2*, 1800156.
[43] T. Kodalle, T. Bertram, R. Schlatmann, C. A. Kaufmann, *IEEE J. Photovoltaics* **2019**, *9*, 1839.
[44] P. Reinhard, B. Bissig, F. Pianezzi, H. Hagendorfer, G. Sozzi, R. Menozzi, C. Gretener, S. Nishiwaki, S. Buecheler, A. N. Tiwari, *Nano Lett.* **2015**, *15*, 3334.
[45] E. Handick, P. Reinhard, R. G. Wilks, F. Pianezzi, T. Kunze, D. Kreikemeyer-lorenzo, L. Weinhardt, M. Blum, W. Yang, M. Gorgoi, E. Ikenaga, D. Gerlach, S. Ueda, Y. Yamashita, T. Chikyow, C. Heske, S. Buecheler, A. N. Tiwari, M. Bär, *ACS Appl. Mater. Interfaces* **2017**, *9*, 3581.
[46] E. Handick, P. Reinhard, J. H. Alsmeier, L. Köhler, F. Pianezzi, S. Krause, M. Gorgoi, E. Ikenaga, N. Koch, R. G. Wilks, S. Buecheler, A. N. Tiwari, M. Bär, *ACS Appl. Mater. Interfaces* **2015**, *7*, 27414.
[47] N. Taguchi, S. Tanaka, S. Ishizuka, *Appl. Phys. Lett.* **2018**, *113*, 113903.

[48] S. Ishizuka, N. Taguchi, P. J. Fons, *J. Phys. Chem. C* **2019**, *123*, 17757.
[49] C. P. Muzzillo, J. D. Poplawsky, H. M. Tong, W. Guo, T. Anderson, *Prog. Photovolt. Res. Appl.* **2018**, *26*, 825.
[50] S. Siebentritt, E. Avancini, M. Bär, J. Bombsch, E. Bourgeois, S. Buecheler, R. Carron, C. Castro, S. Duguay, R. Félix, E. Handick, D. Hariskos, V. Havu, P. Jackson, H. P. Komsa, T. Kunze, M. Malitckaya, R. Menozzi, M. Nesladek, N. Nicoara, M. Puska, M. Raghuwanshi, P. Pareige, S. Sadewasser, G. Sozzi, A. N. Tiwari, S. Ueda, A. Vilalta-Clemente, T. P. Weiss, F. Werner, et al., *Adv. Energy Mater.* **2020**, *10*, 1903752.
[51] N. Nicoara, R. Manaligod, P. Jackson, D. Hariskos, W. Witte, G. Sozzi, R. Menozzi, S. Sadewasser, *Nat. Commun.* **2019**, *10*, 3980.
[52] N. Nicoara, T. Lepetit, L. Arzel, S. Harel, N. Barreau, S. Sadewasser, *Sci. Rep.* **2017**, *7*, 41361.
[53] I. Khatri, H. Fukai, H. Yamaguchi, M. Sugiyama, T. Nakada, *Sol. Energy Mater. Sol. Cells* **2016**, *155*, 280.
[54] A. Laemmle, R. Wuerz, M. Powalla, *Phys. Status Solidi RRL* **2013**, *7*, 631.
[55] O. Ramírez, M. Bertrand, A. Debot, D. Siopa, N. Valle, J. Schmauch, M. Melchiorre, S. Siebentritt, *Sol. RRL* **2021**, *5*, 2000727.
[56] F. Pianezzi, P. Reinhard, A. Chirilă, B. Bissig, S. Nishiwaki, S. Buecheler, A. N. Tiwari, *Phys. Chem. Chem. Phys.* **2014**, *16*, 8843.
[57] C. P. Muzzillo, *Sol. Energy Mater. Sol. Cells* **2017**, *172*, 18.
[58] S. Karki, P. K. Paul, G. Rajan, T. Ashrafee, K. Aryal, P. Pradhan, R. W. Collins, A. Rockett, T. J. Grassman, S. A. Ringel, A. R. Arehart, S. Marsillac, *IEEE J. Photovoltaics* **2017**, *7*, 665.
[59] S. A. Jensen, S. Glynn, A. Kanevce, P. Dippo, J. V. Li, D. H. Levi, D. Kuciauskas, *J. Appl. Phys.* **2016**, *120*, 063106.
[60] S. Zahedi-Azad, M. Maiberg, R. Clausing, R. Scheer, *Thin Solid Films* **2019**, *669*, 629.
[61] S. Ishizuka, N. Taguchi, J. Nishinaga, Y. Kamikawa, S. Tanaka, H. Shibata, *J. Phys. Chem. C* **2018**, *122*, 3809.
[62] J. H. Boyle, B. E. McCandless, W. N. Shafarman, R. W. Birkmire, *J. Appl. Phys.* **2014**, *115*, 223504.
[63] W. Shockley, H. J. Queisser, *J. Appl. Phys.* **1961**, *32*, 510.
[64] T. Kato, J. Wu, Y. Hirai, H. Sugimoto, V. Bermudez, *IEEE J. Photovoltaics* **2019**, *9*, 325.
[65] K. Kim, S. K. Ahn, J. H. Choi, J. Yoo, Y. J. Eo, J. S. Cho, A. Cho, J. Gwak, S. Song, D. H. Cho, Y. D. Chung, J. H. Yun, *Nano Energy* **2018**, *48*, 345.
[66] M. Saad, H. Riazi, E. Bucher, M. C. Lux-steiner, *Appl. Phys. A* **1996**, *62*, 181.
[67] D. L. Young, J. Keane, A. Duda, J. A. M. AbuShama, C. L. Perkins, M. Romero, R. Noufi, *Prog. Photovolt. Res. Appl.* **2003**, *11*, 535.
[68] S. Merdes, R. Mainz, J. Klaer, A. Meeder, H. Rodriguez-Alvarez, H. W. Schock, M. C. Lux-Steiner, R. Klenk, *Sol. Energy Mater. Sol. Cells* **2011**, *95*, 864.
[69] J. Keller, O. V. Bilousov, J. Neerken, E. Wallin, N. M. Martin, L. Riekehr, M. Edoff, C. Platzer-Björkman, *Sol. RRL* **2020**, *4*, 2000248.
[70] J. K. Larsen, F. Larsson, T. Törndahl, N. Saini, L. Riekehr, Y. Ren, A. Biswal, D. Hauschild, L. Weinhardt, C. Heske, C. Platzer-Björkman, *Adv. Energy Mater.* **2019**, *9*, 1900439.
[71] M. Green, E. Dunlop, J. Hohl-Ebinger, M. Yoshita, N. Kopidakis, X. Hao, *Prog. Photovolt. Res. Appl.* **2021**, *29*, 3.
[72] J. A. M. AbuShama, S. Johnston, T. Moriarty, G. Teeter, K. Ramanathan, R. Noufi, *Prog. Photovolt. Res. Appl.* **2004**, *12*, 39.
[73] D. Braunger, T. Duerr, D. Hariskos, C. Koeble, T. Walter, N. Wieser, H. W. Schock, in *25th IEEE Photovolt. Spec. Conf.* **1996**, p. 1001.
[74] K. Siemer, J. Klaer, I. Luck, J. Bruns, R. Klenk, D. Bräunig, *Sol. Energy Mater. Sol. Cells* **2001**, *67*, 159.
[75] W. Wang, M. T. Winkler, O. Gunawan, T. Gokmen, T. K. Todorov, Y. Zhu, D. B. Mitzi, *Adv. Energy Mater.* **2014**, *4*, 1301465.
[76] N. Barreau, A. Thomere, D. Cammilleri, A. Crossay, C. Guillot-Deudon, A. Lafond, N. Stephant, D. Lincot, M. T. Caldes, R. Bodeux, B. Berenguier, in *47th IEEE Photovolt. Spec. Conf.* **2020**, p. 1715.
[77] P. Jackson, D. Hariskos, R. Wuerz, W. Wischmann, M. Powalla, *Phys. Status Solidi RRL* **2014**, *8*, 219.
[78] F. Larsson, O. Donzel-Gargand, J. Keller, M. Edoff, T. Törndahl, *Sol. Energy Mater. Sol. Cells* **2018**, *183*, 8.
[79] D. W. Niles, K. Ramanathan, F. Hasoon, R. Noufi, B. J. Tielsch, J. E. Fulghum, *J. Vac. Sci. Technol., A* **1997**, *15*, 3044.
[80] R. Davidovich, P. Fedorov, A. Popov, *Rev. Inorg. Chem.* **2017**, *37*, 147.
[81] J. Keller, N. Shariati Nilsson, A. Aijaz, L. Riekehr, T. Kubart, M. Edoff, T. Törndahl, *Prog. Photovolt. Res. Appl.* **2018**, *26*, 159.
[82] J. Keller, W.-C. Chen, L. Riekehr, T. Kubart, T. Törndahl, M. Edoff, *Prog. Photovolt. Res. Appl.* **2018**, *26*, 846.
[83] N. Maticiuc, T. Kodalle, J. Lauche, R. Wenisch, T. Bertram, C. A. Kaufmann, I. Lauermann, *Thin Solid Films* **2018**, *665*, 143.
[84] M. Raghuwanshi, A. Vilalta-Clemente, C. Castro, S. Duguay, E. Cadel, P. Jackson, D. Hariskos, W. Witte, P. Pareige, *Nano Energy* **2019**, *60*, 103.
[85] P. Schöppe, S. Schönherr, P. Jackson, R. Wuerz, W. Wisniewski, M. Ritzer, M. Zapf, A. Johannes, C. S. Schnohr, C. Ronning, *ACS Appl. Mater. Interfaces* **2018**, *10*, 40592.
[86] T. Y. Lin, I. Khatri, J. Matsuura, K. Shudo, W. C. Huang, M. Sugiyama, C. H. Lai, T. Nakada, *Nano Energy* **2020**, *68*, 104299.
[87] P. Schöppe, S. Schönherr, M. Chugh, H. Mirhosseini, P. Jackson, R. Wuerz, M. Ritzer, A. Johannes, G. Martínez-Criado, W. Wisniewski, T. Schwarz, C. T. Plass, M. Hafermann, T. D. Kühne, C. S. Schnohr, C. Ronning, *Nano Energy* **2020**, *71*, 104622.
[88] J. Keller, F. Chalvet, J. Joel, A. Aijaz, T. Kubart, L. Riekehr, M. Edoff, L. Stolt, T. Törndahl, *Prog. Photovolt. Res. Appl.* **2018**, *26*, 13.
[89] M. Malitckaya, H. P. Komsa, V. Havu, M. J. Puska, *J. Phys. Chem. C* **2017**, *121*, 15516.
[90] C. P. Muzzillo, L. M. Mansfield, K. Ramanathan, T. J. Anderson, *J. Mater. Sci.* **2016**, *51*, 6812.
[91] T. P. Weiss, S. Nishiwaki, B. Bissig, R. Carron, E. Avancini, J. Löckinger, S. Buecheler, A. N. Tiwari, *Adv. Mater. Interfaces* **2018**, *5*, 1701007.
[92] G. Sozzi, S. DI Napoli, M. Enna, R. Menozzi, in *46th IEEE Photovolt. Spec. Conf.* **2019**, p. 953.
[93] T. Schwarz, G. Stechmann, B. Gault, O. Cojocaru-Mirédin, R. Wuerz, D. Raabe, *Prog. Photovolt. Res. Appl.* **2018**, *26*, 196.
[94] P. Schöppe, S. Schönherr, R. Wuerz, W. Wisniewski, G. Martínez-Criado, M. Ritzer, K. Ritter, C. Ronning, C. S. Schnohr, *Nano Energy* **2017**, *42*, 307.
[95] R. Wuerz, W. Hempel, P. Jackson, *J. Appl. Phys.* **2018**, *124*, 165305.
[96] H. Aboulfadl, K. V. Sopiha, J. Keller, J. K. Larsen, J. J. S. Scragg, C. Persson, M. Thuvander, M. Edoff, *ACS Appl. Mater. Interfaces* **2021**, *13*, 7188.
[97] M. Chugh, T. D. Kühne, H. Mirhosseini, *ACS Appl. Mater. Interfaces* **2019**, *11*, 14821.
[98] J.-H. Yoon, J.-H. Kim, W. M. Kim, J.-K. Park, Y.-J. Baik, T.-Y. Seong, J. Jeong, *Prog. Photovolt. Res. Appl.* **2014**, *22*, 90.
[99] D. Abou-Ras, B. Marsen, T. Rissom, F. Frost, H. Schulz, F. Bauer, V. Efimova, V. Hoffmann, A. Eicke, *Micron* **2012**, *43*, 470.
[100] J. E. Avon, K. Yoodee, J. C. Woolley, *J. Appl. Phys.* **1984**, *55*, 524.
[101] K. V. Sopiha, J. K. Larsen, O. Donzel-Gargand, F. Khavari, J. Keller, M. Edoff, C. Platzer-Björkman, C. Persson, J. J. S. Scragg, *J. Mater. Chem. A.* **2020**, *8*, 8740.
[102] A. Stokes, M. Al-Jassim, A. Norman, D. Diercks, B. Gorman, *Prog. Photovolt. Res. Appl.* **2017**, *25*, 764.
[103] A. Vilalta-Clemente, M. Raghuwanshi, S. Duguay, C. Castro, E. Cadel, P. Pareige, P. Jackson, R. Wuerz, D. Hariskos, W. Witte, *Appl. Phys. Lett.* **2018**, *112*, 103105.